

RESEARCH ARTICLE

10.1002/2017JD027836

Key Points:

- Satellite remote sensors are critical for constraining carbon cycle processes
- Active remote sensing shows the potential to provide a stronger constraint than passive remote sensing
- Regional flux perturbations are detectable at the annual and seasonal scales with sufficient precision even in the presence of model errors

Supporting Information:

- Supporting Information S1

Correspondence to:

S. M. R. Crowell,
scrowell@ou.edu

Citation:

Crowell, S. M. R., Randolph Kawa, S., Browell, E. V., Hammerling, D. M., Moore, B., Schaefer, K., & Doney, S. C. (2018). On the ability of space-based passive and active remote sensing observations of CO₂ to detect flux perturbations to the carbon cycle. *Journal of Geophysical Research: Atmospheres*, 123, 1460–1477. <https://doi.org/10.1002/2017JD027836>



Received 3 OCT 2017

Accepted 29 DEC 2017

Accepted article online 9 JAN 2018

Published online 29 JAN 2018

On the Ability of Space-Based Passive and Active Remote Sensing Observations of CO₂ to Detect Flux Perturbations to the Carbon Cycle

Sean M. R. Crowell¹ , S. Randolph Kawa², Edward V. Browell³ , Dorit M. Hammerling⁴ , Berrien Moore¹, Kevin Schaefer⁵ , and Scott C. Doney^{6,7} 

¹College of Atmospheric and Geographic Sciences, University of Oklahoma, Norman, OK, USA, ²NASA Goddard Space Flight Center, Greenbelt, MD, USA, ³STARSS-III Affiliate, NASA Langley Research Center, Hampton, VA, USA, ⁴Institute for Mathematics Applied to Geosciences, National Center for Atmospheric Research, Boulder, CO, USA, ⁵National Snow and Ice Data Center, Cooperative Institute for Research in Environmental Sciences, University of Colorado Boulder, Boulder, CO, USA, ⁶Department of Marine Chemistry and Geochemistry, Woods Hole Oceanographic Institution, Woods Hole, MA, USA, ⁷Department of Environmental Sciences, University of Virginia, Charlottesville, VA, USA

Abstract Space-borne observations of CO₂ are vital to gaining understanding of the carbon cycle in regions of the world that are difficult to measure directly, such as the tropical terrestrial biosphere, the high northern and southern latitudes, and in developing nations such as China. Measurements from passive instruments such as GOSAT and OCO-2, however, are constrained by solar zenith angle limitations as well as sensitivity to the presence of clouds and aerosols. Active measurements such as those in development for the Active Sensing of CO₂ Emissions over Nights, Days and Seasons (ASCENDS) mission show strong potential for making measurements in the high-latitude winter and in cloudy regions. In this work we examine the enhanced flux constraint provided by the improved coverage from an active measurement such as ASCENDS. The simulation studies presented here show that with sufficient precision, ASCENDS will detect permafrost thaw and fossil fuel emissions shifts at annual and seasonal time scales, even in the presence of transport errors, representativeness errors, and biogenic flux errors. While OCO-2 can detect some of these perturbations at the annual scale, the seasonal sampling provided by ASCENDS provides the stronger constraint.

Plain Language Summary Active and passive remote sensors show the potential to provide unprecedented information on the carbon cycle. With the all-season sampling, active remote sensors are more capable of constraining high-latitude emissions. The reduced sensitivity to cloud and aerosol also makes active sensors more capable of providing information in cloudy and polluted scenes with sufficient accuracy. These experiments account for errors that are fundamental to the top-down approach for constraining emissions, and even including these sources of error, we show that satellite remote sensors are critical for understanding the carbon cycle.

1. Introduction

Interactions between the global carbon cycle and the climate system remain a key uncertainty in predictions of future climate (Friedlingstein et al., 2014). A significant difficulty is the lack of atmospheric CO₂ observations and surface flux characterization in regions that are likely to be most susceptible to climatic change, such as the Northern Hemisphere (NH) permafrost regions, tropical forests, and the Southern Ocean. These concerns led to the development of space-based remote sensors, examples being the Greenhouse Gas Observing Satellite (GOSAT) (Kuze et al., 2016) and the Orbiting Carbon Observatory 2 (OCO-2) (Crisp et al., 2004).

OCO-2 successfully launched into a low Earth orbit (LEO) in July 2014 and has gathered data continuously in glint, nadir, and target viewing geometries since August 2014. OCO-2 measures sunlight reflected from the surface of the Earth in three bands: the O₂ A band (0.76–0.77 μm), the weak CO₂ (WCO₂) band (1.59–1.62 μm), and the strong CO₂ (SCO₂) band (2.04–2.09 μm). These measurements are then used to retrieve the CO₂ column dry-air mole fraction (X_{CO_2}) using a full physics radiative transfer model coupled to an

iterative least squares optimization scheme, such as the Atmospheric Carbon Observing System (ACOS) algorithm (O'Dell et al., 2012). Previous studies suggest that if OCO-2 provides measurements of X_{CO_2} at the expected precision of 0.5 to 1 ppm (Boesch et al., 2011), the uncertainties on inferred CO_2 surface fluxes will be substantially reduced at regional and continental scales (Baker et al., 2010; Miller et al., 2007; Rayner & O'Brien, 2001).

Over 2 years of data from OCO-2 now show a need to revisit the expectations of earlier studies (Baker et al., 2010; Boesch et al., 2011). The actual number of daily soundings with successful retrievals is smaller than predicted due to (1) more stringent than expected solar zenith angle limitations, (2) topographic variability, and (3) more soundings than expected failing to pass the cloud postscreening tests in the retrieval algorithm (C. O'Dell, private communication, 2017). Thus, cloudier regions of the globe such as the Amazon have few retrievals over large areas. Additionally, retrievals of X_{CO_2} over snow and ice have proven difficult due to low signal. Eldering et al. (2017) states that actual single-sounding errors are about double the reported uncertainties. Kulawik et al. (2015) find that aggregation of multiple GOSAT soundings reduces errors relative to Total Carbon Column Observing Network (TCCON), but a nonzero "noise floor" serves as a lower bound as the number of samples increases. Similar results have been obtained for OCO-2 (S. Kulawik, private communication, 2017). This points to residual systematic error in the bias-corrected OCO-2 X_{CO_2} , which the OCO-2 Users Guide (NASA, 2015) suggests can be significant for soundings with air mass factors larger than 2.5. Analysis by Wunch et al. (2017) computes biases in OCO-2 observations relative to individual TCCON sites and confirms that residual biases remain that vary by site and season. All of these differences between the expected instrument performance (Boesch et al., 2011) and the actual performance point to a need to revisit the conclusions of Baker et al. (2010) regarding CO_2 flux uncertainty reduction.

These considerations strengthen the case for active remote sensing as an approach to measuring trace gases from space. Gas measurements with active sensors are insensitive to the presence of aerosols due to their high spectral resolution sampling of narrow absorption features, over which aerosol effects are effectively constant. The path length (i.e., air mass factor) and height of scattering layers are precisely measured products of the technique, which removes potential sources of bias. Additionally, as both the transmitted and received signal wavelengths and amplitudes are measured with a high degree of accuracy, more robust statistical (i.e., based on photon counting) error estimates are possible.

The Active Sensing of CO_2 Emissions over Nights, Days and Seasons (ASCENDS) mission was recommended by the National Research Council in the 2007 Earth Science and Applications from Space Decadal Survey (National Research Council, 2007) to complement planned passive CO_2 missions. The recommendation was driven by the need to observe CO_2 with measurements at all latitudes, day, and night. The expectation at the time was that diurnal measurements should disentangle gross primary productivity (GPP) and respiration (Re) processes at the global scale, which is a major goal of space-based remote sensing of CO_2 , though this has not been borne out by subsequent studies, such as Kawa et al. (2010).

Since the National Research Council report, instrument design teams at NASA centers have proposed candidate lidar instruments with different approaches that utilize CO_2 absorption lines in the 1.57 μm WCO₂ band or the 2.05 μm SCO₂ band. Numerous field tests using airborne simulator instruments have demonstrated the ability of the active lidar measurements to retrieve column CO_2 fraction (X_{CO_2}) with high precision (e.g., Abshire et al., 2010, 2014; Browell et al., 2008, 2009, 2010; Dobler et al., 2013; Menzies et al., 2013; Spiers et al., 2011) over various surface types and atmospheric conditions. Low bias is expected, but to date the airborne instruments have not demonstrated this capability. In addition, recent work has shown that in the presence of optically thick clouds, cloud top retrievals of X_{CO_2} show a potential for separating free tropospheric CO_2 from the CO_2 in the planetary boundary layer (PBL) (Lin et al., 2015; Mao et al., 2018; Ramanathan et al., 2015), which should yield strong constraints on surface fluxes of CO_2 .

Several observing system simulation experiments (OSSEs) have been performed by the ASCENDS ad hoc Science Definition Team (SDT). Kawa et al. (2010) and ASCENDS SDT (Jucks et al., 2015) showed that lidar measurements have potential for constraining fluxes due to the high signal-to-noise ratios (SNRs), where the random errors in the measurements were computed using attenuation of the lidar beam due to clouds and aerosols and surface reflectance variations. However, the difference in X_{CO_2} at dawn and dusk was found to be comparable or smaller than the noise in the measurements for the nominal instrument model of

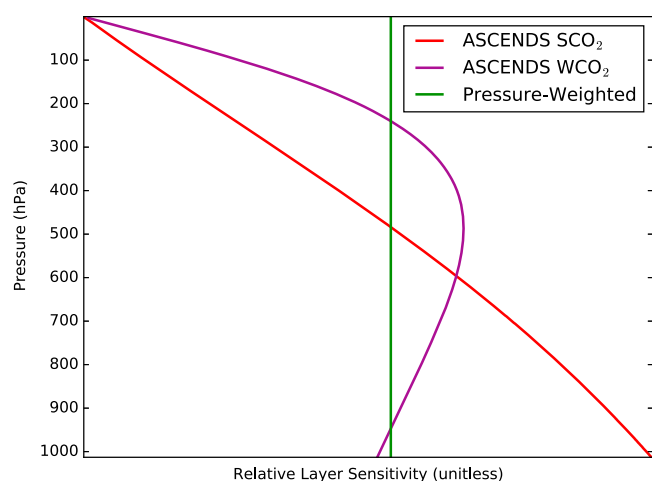


Figure 1. The normalized weighting functions used in the OSSE studies to produce column-integrated CO₂. These weighting function are calculated via (2) using a U.S. standard atmosphere. The green line denotes a pressure-weighted averaging kernel, which was used for OCO-2 simulations.

that time. The authors concluded that it was unlikely that a dawn-dusk orbit would constrain the diurnal cycle, which is linked to separating sinks from photosynthesis during the day and sources from respiration at night. Wang et al. (2014) employed a synthesis inversion framework and demonstrated the capability of ASCENDS observations to provide significant uncertainty reductions on regional scale fluxes. This work included the first relative comparison of CO₂ measurements from different ASCENDS instrument concepts to constrain fluxes and found that under the same assumed measurement precisions and in the absence of transport error, the SCO₂ instrument concept provided a somewhat stronger flux constraint due to its greater sensitivity nearer the surface (Figure 1).

Hammerling et al. (2015, hereafter H15) revisited the detectability of carbon flux signals first addressed in Kawa et al. (2010) using ASCENDS WCO₂ pseudodata. Based on the statistical significance of the detected X_{CO2} signal above the instrument and sampling noise, H15 found that ASCENDS would be able to detect three specific perturbations to global CO₂ emissions: permafrost thaw, neutral fossil fuel emissions shift from Europe to China, and interannual variability in the Southern Ocean.

The cases of permafrost thawing and large regional change in fossil fuel emissions were detected with some spatial discrimination and 3 months of averaging. H15 further concluded that ASCENDS would not be able to detect spatial gradients in the Southern Ocean basins, though it would detect changes in the total over the region.

In this study, we extend the inferences about fossil fuel pattern shifts, permafrost thaw, and Southern Ocean interannual variability discussed in H15 in two ways. First, we utilize the pseudodata to directly estimate fluxes in an inversion framework. Second, we include comparisons of flux estimates constrained with pseudodata modeled on passive measurements, as well as a SCO₂ active measurement. With these extensions, we address whether an active measurement like ASCENDS would be able to match or improve upon the flux constraint provided by a passive measurement like OCO-2.

The paper proceeds as follows. In section 2.1, we present the flux inversion framework, TM5-4DVAR. Section 2.2 details the creation of pseudodata for the passive and active instruments. Section 2.3 presents the flux perturbation scenarios. Results of the flux inversion experiments are discussed in section 3, and section 4 presents discussion and conclusions.

2. Experiment Design

Here we present the different components of the experimental setup, including the transport model and data assimilation frameworks, as well as the observation operator and error specification for both the ASCENDS and OCO-2 pseudodata. We discuss the methods for simulating OCO-2 (section 2.2.1) and ASCENDS (section 2.2.2) observations and then discuss transport (section 2.2.3) and representativeness (section 2.2.4) errors. The uncertainties of the aggregated XCO₂ measurements are presented in section 2.2.5.

2.1. TM5-4DVAR

The flux inversion framework described by Basu et al. (2013) is utilized in these experiments. The transport model TM5 (Krol et al., 2005) is employed to predict the 4-D field of CO₂ mixing ratio that results from surface emissions and atmospheric transport produced by the ERA-Interim meteorological reanalysis (Dee et al., 2011). TM5 has been used in numerous studies and forms the backbone of the Carbon Tracker (Peters et al., 2007) suite of flux products and diagnostics produced by NOAA. An adjoint model was developed for the multitracer passive tracer transport model in TM5, and this enables the optimal estimation of fluxes from concentration measurements using gradient-based algorithms, such as the conjugate gradient method. The capabilities of the Four-Dimensional Variational (4DVAR) method that employs the gradient-based minimization have been demonstrated by Basu et al. (2013) and Babenhauserheide et al. (2015). The 4DVAR seeks

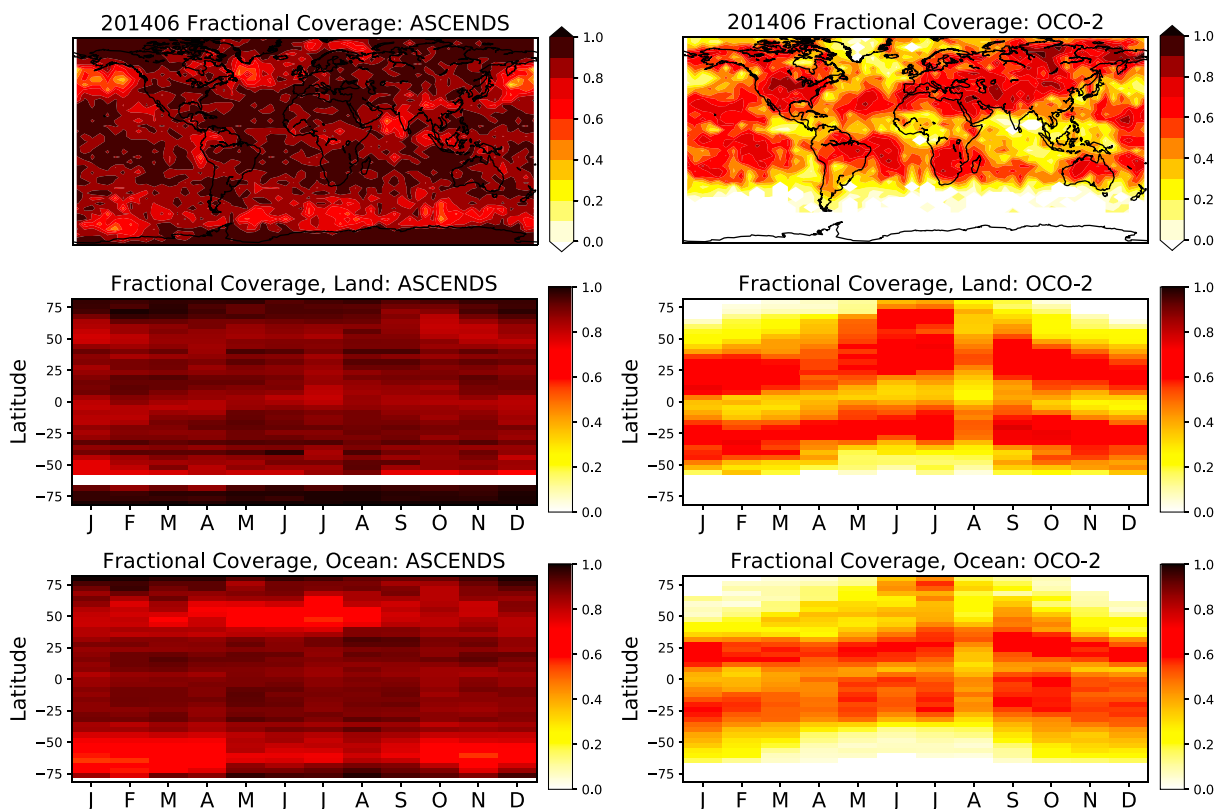


Figure 2. The fractional coverage of each 6×4 gridbox of soundings by each instrument, defined by the number of $1^\circ \times 1^\circ$ gridboxes that contain at least one 10 s average (equivalently, one sounding for OCO-2 or one 5 km sounding for ASCENDS) within a given month out of a total of 24 possible. (top row) The spatial distribution for June and (middle and bottom rows) zonal averages by month. The seasonally varying coverage of OCO-2 is evident in these plots, as is the ability of ASCENDS to make observations through thin clouds ($OD < 1.0$). This number is used to scale the representativeness error in Figure 3. White pixels represent months and latitudes in which there are no soundings.

the surface flux field that, when used to drive TM5 forward, best matches the observations within their relative uncertainties, over a long observational “window.” The long window means that fluxes are informed by observations that may occur far afield. The analysis in H15 addresses aggregated concentration differences that do not distinguish the varying long-term transport impacts, and thus, we expect the conclusions here to be stronger than those in H15.

Posterior uncertainties are estimated using equation (8) of Meirink et al. (2008), which reconstructs the covariances based on the eigenvalues and eigenvectors that are products of the Lanczos implementation of the conjugate gradient algorithm. The uncertainty arising from this approximation is an overestimate of the true posterior uncertainty.

2.2. Pseudodata and Uncertainties

Satellite observation operators for TM5 were discussed by Basu et al. (2013), and we employ those same operators. Assimilating satellite data with TM5-4DVAR requires an averaging kernel, a column average mixing ratio, and an uncertainty, specified as a standard deviation, for each sounding. Briefly, the model applies a user-defined averaging kernel (i.e., the sensitivity of the retrieval to different atmospheric layers) to the model profile of CO_2 mixing ratio and so computes the model-predicted X_{CO_2} . The difference between this model-predicted X_{CO_2} and the observed value, scaled by the observational uncertainty, is then propagated through the adjoint to compute flux corrections.

In the spirit of Baker et al. (2010), observations from each of the measurement approaches are aggregated to the model grid resolution (6° longitude by 4° latitude, Figure 2). The aggregated “observation” is treated as the mean X_{CO_2} for that grid box and must be assigned an appropriate uncertainty. We include estimates of

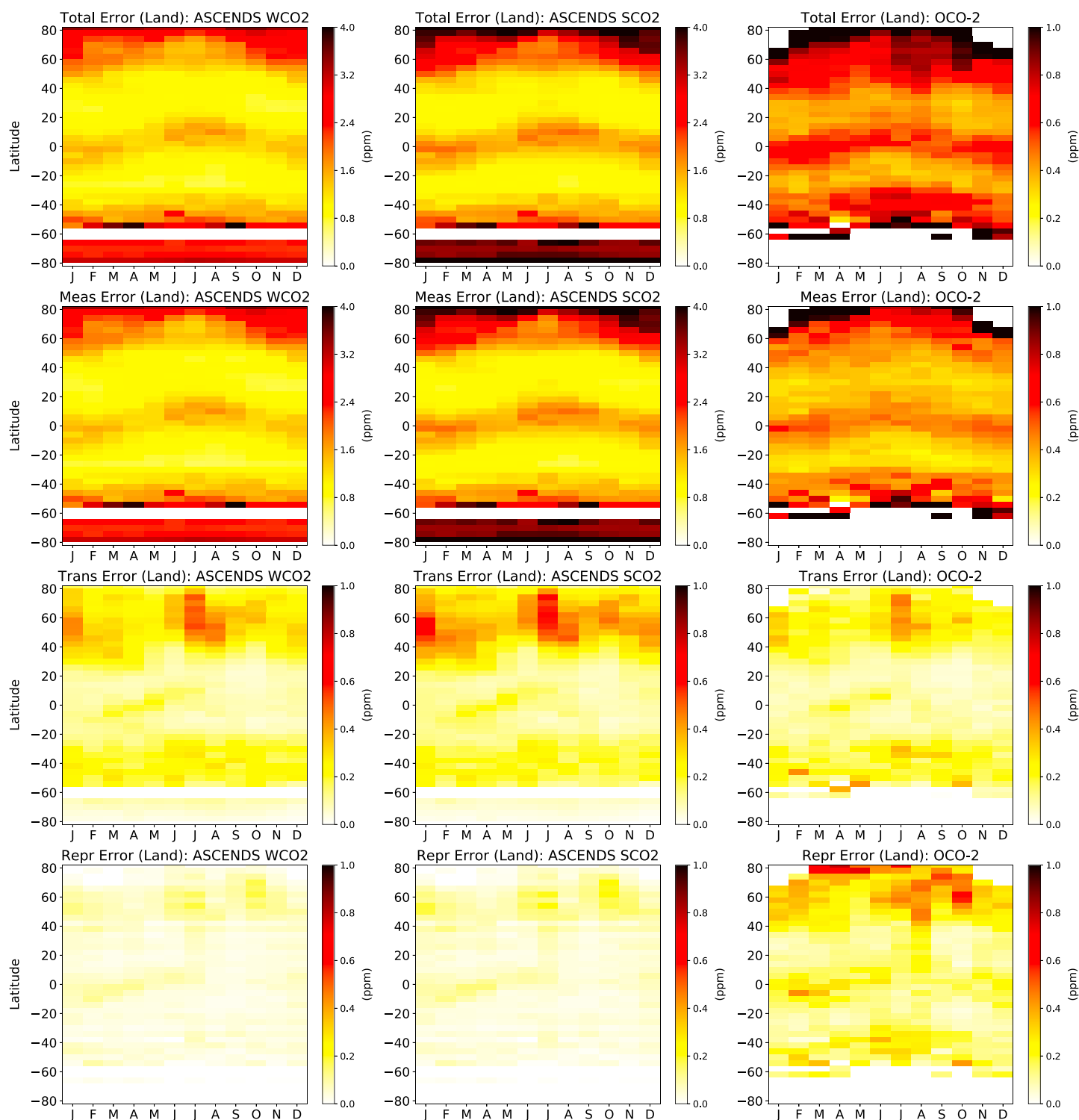


Figure 3. Zonal mean of errors over land used in the inversion experiments. (second row) Measurement errors are derived as described in the text. (third row) Transport errors in XCO₂ are computed from 18 h lagged simulations. From the images above the covariance between fluxes and transport is apparent, with maxima in the errors during the peak drawdown season. (fourth row) Representativeness errors were computed using differences between XCO₂ simulated using fluxes and meteorology at $1^\circ \times 1^\circ$ and $6^\circ \times 4^\circ$ resolution, scaled by the fraction of the grid box not sampled as depicted in Figure 2, with an additional 0.2 ppm in line with Corbin et al. (2008) combined in quadrature. For both transport and representativeness errors, the peaking of the ASCENDS SCO₂ instrument's weighting function results in increased errors. Note the difference in scales for the first and second rows between ASCENDS (maximum of 4 ppm) and OCO-2 (maximum of 1 ppm), as the measurement errors for ASCENDS are larger due to SNR and the number of soundings. White pixels represent latitudes and months in which there were no soundings.

single-sounding precision, representativeness error, and transport error in our uncertainty at grid scale. There are no systematic error assumptions present in our simulations. We make this concession due to a very limited understanding of systematic errors in both passive and active instruments, with the understanding that these findings will be revised as more findings on systematic errors come to light.

2.2.1. OCO-2 Simulated Data

OCO-2 observes a narrow swath composed of eight “footprints” across its 10 km track, each of which is nominally 2 km wide. Individual footprints are reported as independent soundings, and so the potential exists for eight independent pixels across track per 2 km of orbit track or ~300 soundings per 10 s along track. The actual number of successfully retrieved soundings is less than this due to clouds and aerosols. The OCO-2 Version 7B lite files for 2016 were employed for the satellite track and single-sounding uncertainty information, as this time period is wholly composed of the updated sampling that alternates nadir and glint modes on each orbit. All nadir and glint soundings with a quality flag of 0 were used. Note that this implicitly eliminates scenes that are contaminated by clouds and aerosols, because those soundings are flagged by the preprocessing algorithms and are not run through the retrieval algorithm. Naturally, there are situations in which the prescreening will miss clouds, and so we only use the soundings marked as “good” via the quality flag, since comparisons with other satellite-derived cloud products show that OCO-2 preprocessing screens out cloudy scenes with sufficiently high accuracy (Taylor et al., 2016).

Kulawik et al. (2015) showed that when aggregating multiple soundings over the same spatial footprint, the root-mean-square difference between GOSAT observations and TCCON does not asymptotically approach 0 as the number of soundings increases, indicating the presence of correlated random errors and/or systematic errors in the single-sounding values. To account for this in our experiments, we inflate the reported single-sounding uncertainty σ_i with an adaptive scale factor α_i given by

$$\alpha_i = 1 + 0.6^2 \sum \sigma_j^{-2} \quad (1)$$

so that over any 10 s period, the mean X_{CO_2} has an uncertainty of no less than 0.6 ppm (the values σ_j are twice the reported uncertainties (Worden et al., 2017) of the other soundings in the 10 s period). This inflation accounts for correlations between the errors of neighboring soundings and avoids overly optimistic uncertainties for single OCO-2 soundings.

The 10 s averages are aggregated to 6° by 4° grid boxes and their errors combined using inverse variance weighting, which assumes that 10 s averages are independent. The 6° by 4° uncertainties are plotted in Figures 3 and 4 as zonal monthly averages for land and ocean, respectively.

2.2.2. ASCENDS

Assuming an A-Train orbit, a good proxy for the ASCENDS orbit track and ground sampling (latitude, longitude, and date) is the Cloud-Aerosol Lidar and Infrared Pathfinder Satellite Observation (CALIPSO; Garnier et al., 2012; Hunt et al., 2009; Winker et al., 2013). For each ASCENDS instrumental approach, we approximate the vertical averaging kernel with the instrument weighting function (WF), which is accurate assuming a single online and a single off-line measured absorption. The weighting function is given in pressure coordinates by

$$\text{WF}(p) = \frac{\Delta \epsilon^\zeta(p)}{m_d g(p) \left(1 + q_{\text{H}_2\text{O}}(p) \frac{m_{\text{H}_2\text{O}}}{m_d} \right)} \quad (2)$$

where m_d is the molar mass of dry air, g is the local gravitational acceleration, $q_{\text{H}_2\text{O}}$ is the water vapor dry air mole fraction, and $m_{\text{H}_2\text{O}}$ is the molar mass of water vapor. The differential absorption cross section $\Delta \epsilon^\zeta$ is a function of atmospheric temperature, humidity, and pressure, as well as the spectral absorption feature sampled by the lidar. Sample WFs for a WCO₂ and SCO₂ lidar, computed using the U.S. Standard Atmosphere, are shown in Figure 1. Of particular interest is the location of the peak of each WF, which signifies which layer of the atmosphere has the most influence on the retrieved X_{CO_2} . Since the 2 μm WF peaks at the surface, we expect that the retrieved column mixing ratios are more sensitive to variations in sources and sinks near the surface, while the 1.57 μm WF better captures the integrated CO₂ column across the entire troposphere. If the uncertainties in both instruments were identical, the expectation is that the 2 μm instrument would provide a larger flux uncertainty reduction in the absence of transport errors, particularly those in vertical mixing.

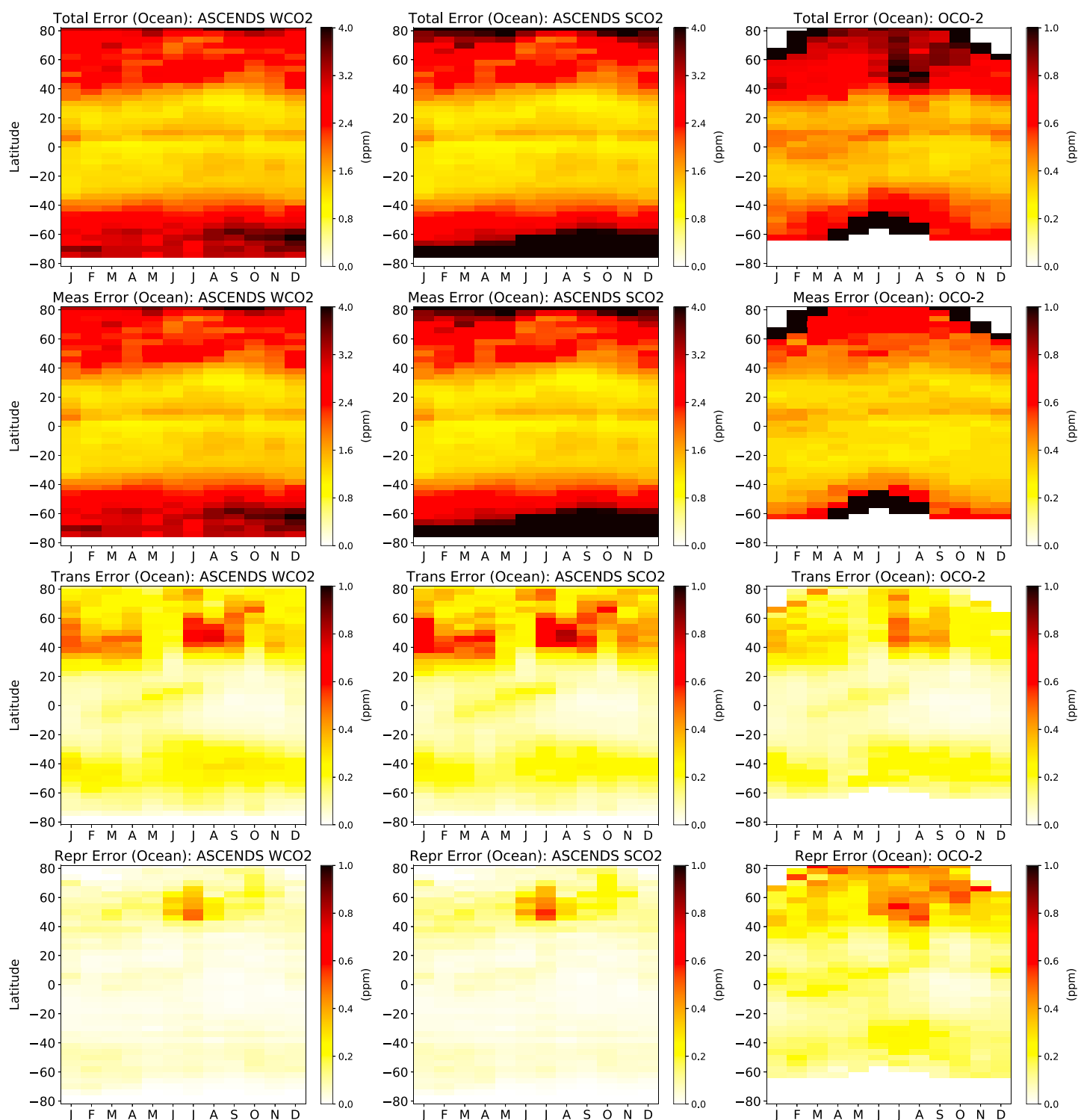


Figure 4. As in Figure 3 but for zonal average errors over the ocean. Note that the color scales in the first and second rows are different for ASCENDS and OCO-2 nadir and glint observations, given the larger measurement errors for ASCENDS (maximum 4 ppm) relative to OCO-2 (maximum 1 ppm).

Uncertainty in ASCENDS-sampled X_{CO_2} is prescribed as in H15, Kawa et al. (2010), and Jucks et al. (2015) and is described briefly here. The nominal ASCENDS observation is made at a 0.1 s interval, with precision prescribed for a 10 s average of X_{CO_2} along track that is computed as follows. Each 10 s average is composed of 10 to 15 5 km sections of orbit matching the CALIPSO cloud and aerosol optical depth (OD) products. CALIPSO OD products use 5 km aggregates of 333 m soundings to improve the accuracy of the OD retrieval. The precision for a 5 km scene is given by

$$\sigma_{5\text{km}} = \frac{3.667\sigma_{\text{ref}}}{\sqrt{\beta T^2 f / \beta_{\text{ref}}}}. \quad (3)$$

Instrument noise is modeled assuming a baseline reference instrument precision σ_{ref} of 1.0 ppm for a 10 s average X_{CO_2} . The reference conditions are a clear scene (aerosol and cloud OD = 0) and a surface lidar backscatter β_{ref} of 0.176 sr⁻¹ for 1.57 μm and 0.161 sr⁻¹ for 2 μm , which approximate conditions at Railroad Valley, Nevada. The reference precision of 1.0 ppm was chosen in line with the conclusions of Miller et al. (2007), who stated a precision requirement of 1–2 ppm to constrain large-scale sources and sinks. More recent ASCENDS flight campaigns have shown (Browell et al., 2010; Dobler et al., 2013) that 10 s average precision of $\sigma_{\text{ref}}=0.5$ ppm or less is readily attainable. We also perform experiments labeled 2P and 4P that utilize a reference precision of $\sigma_{\text{ref}}=0.5$ ppm and $\sigma_{\text{ref}}=0.25$ ppm, respectively.

The wavelength-dependent surface backscatter β is computed using the glint formulation of Hu et al. (2008) over water with MERRA 10 m wind speeds and from the MODIS 5 km 16 day nadir bidirectional reflectance data in bands 6 and 7 (Schaaf et al., 2002) for WCO₂ and SCO₂, respectively, over land. In general, reflectance is lower for SCO₂ than for WCO₂, which leads to larger uncertainties. The local one-way transmittance is $T = e^{-\text{OD}}$, where OD is the CALIPSO 5 km total aerosol plus cloud OD. The quantity f gives the frequency of detectable surface returns (i.e., useable data) in the 5 km average and hence falls between 0 and 1 (inclusive). Soundings with an OD greater than 1.0 were not included in the sample set, as a crude quality filter. The 5 km precision values based on these quantities are aggregated to 10 s inverse variance weighted averages to match the expected sampling measurement requirements as discussed in Jucks et al. (2015).

2.2.3. Transport Errors

In order to avoid overly optimistic results, we must account for the impacts of transport error (Chevallier et al., 2010) on flux estimates. In general, this is a difficult quantity to estimate, and in this work we follow the approach of Baker et al. (2010), where forward simulations of X_{CO_2} are performed for each instrument with a lag time of 18 h relative to the reference simulation, and the statistics of the differences are used as a proxy for synoptic scale transport uncertainty. The RMS of the differences is computed monthly at the resolution of the inversion calculations, and the monthly means by latitude and surface type are displayed in Figures 3 and 4. For all instruments, the summer drawdown in the Northern Hemisphere leads to a larger error, indicating the covariance between fluxes and atmospheric transport as signals in X_{CO_2} . Interestingly, the ASCENDS SCO₂ instrument's surface peaked weighting function leads to a larger transport error, likely due to the boundary layer errors induced by the lagged difference estimate. Conversely, the OCO-2 pure pressure-weighted X_{CO_2} is the least sensitive to transport differences.

In line with the conclusions of Chevallier et al. (2010), we enforce transport errors as irreducible at the 6° by 4° grid scale (i.e., without dependence on the number of soundings), as they found similar transport effects when using a much reduced data set as those using the full set of observations.

2.2.4. Representativeness Errors

Given that both OCO-2 and ASCENDS are narrow swath measurements, we must account for the fact that individual soundings are not representative of the much coarser model grid. This topic was addressed in Corbin et al. (2008), where the authors utilized simulated OCO retrievals to connect individual soundings to coarser grid boxes. They found that these errors are random in nature and can be modeled with a Gaussian distribution. Baker et al. (2010) estimated this error by converting flux magnitude at 1° by 1° into X_{CO_2} uncertainty with a fixed scale factor, indicative of the fact that representativeness error is dominated by the underlying fluxes. We take a slightly different approach. We perform a forward simulation at both 1° by 1° and at 6° by 4° (longitude by latitude) and sample the model concentrations as OCO-2 and ASCENDS. We treat the differences in the simulated soundings as estimates of the representativeness error

and compute the mean absolute error for each 6° by 4° grid box for each month. This mean is scaled by the number of 1° by 1° that are *not sampled* in a given month. The fractional coverage of OCO-2 and ASCENDS are displayed in Figure 2, where it is clear that the lidar sampling approach avoids the majority of the issues related to cloud cover by sampling through thin clouds ($OD < 1.0$) and also by sampling at night. This more representative sampling leads to much smaller representativeness errors in Figures 3 (fourth row) and 4 (fourth row).

To account for the extra error arising from the track to 1° by 1° grid box, we add an additional constant error of 0.2 ppm from Corbin et al. (2008) to the larger-scale error in quadrature. This assumes that the representativeness of ASCENDS and OCO-2 on the smallest scales is the same. Given the lack of knowledge of the behavior of X_{CO_2} variations on the scales between 300 m and 2 km, this is a fair assumption. Current field campaigns such as ACT America will shed light on this issue with onboard lidar instruments and OCO-2 underflights, but the results of these studies are not presently available.

2.2.5. Total Uncertainty

The uncertainty for the grid scale X_{CO_2} at 6° by 4° is computed by summing contributions from instrument precision (retrieval error), transport, and representativeness errors in quadrature. The zonal averages by month of the total errors are displayed in Figures 3 (first row) and 4 (first row). As expected, the total errors for ASCENDS are dominated by the measurement component for the nominal case. For the higher-precision cases, this component reduces by the appropriate factor (i.e., 2 for 2P and 4 for 4P) and the other components of the error budget become a larger fraction of the errors, since they are not dependent on the instrument precision. For the highest-precision cases, labeled in later sections as 4P, ASCENDS and OCO-2 have comparable total errors.

2.2.6. Systematic Measurement Errors

Systematic errors can result in large biases in estimated surface fluxes (Engelen et al., 2002). However, modeling these biases is ad hoc and beyond the scope of what we hope to achieve here, which is demonstrating the impacts of sampling and random error differences on posterior flux errors.

2.3. Flux Scenarios

In each experiment, truth fluxes are created by layering a flux perturbation over a set of baseline climatological emissions. We describe two sets of baseline emissions first, followed by the different perturbations. The baseline emissions are different from those in H15, but the perturbations are identical.

2.3.1. Baseline Surface Fluxes

H15 employed a signal detection strategy to determine whether ASCENDS would be able to “see” perturbations to the carbon cycle. Their approach was to layer a perturbation over a baseline set of fluxes. Here we expand on that idea by using two different sets of biogenic fluxes, one of which is treated as the “true” baseline and the other as a “biased” baseline. The pseudodata are simulated using the true baseline, while the biased baseline is used as the prior in the inversion experiments. The posterior uncertainty from each observation type with only the biological flux signal gives a measure of the ability of the satellites to constrain the biogenic fluxes within the current uncertainty in carbon cycle studies. This enables conclusions that encapsulate the current state of knowledge of the carbon cycle as part of the uncertainty that new observations must overcome to enable a true advancement to our understanding.

The true baseline is composed of biospheric fluxes and fire emissions taken from the Carnegie-Ames-Stanford Approach-Global Fire Emissions Database version 3 (CASA-GFEDv3) project, climatological ocean fluxes from Takahashi et al. (2009), which are estimated from measurements of pCO_2 on ocean cruises, and fossil fuel emissions taken from the Open-source Data Inventory for Anthropogenic CO_2 (ODIAC, Oda & Maksyutov, 2011). The “biased” baseline uses the same fire and fossil fuel emissions but replaces the net ecosystem CO_2 exchange (NEE) from CASA with NEE from the Simple Biosphere model, Version 4 (SiB4) and the ocean fluxes from Takahashi with those from the Biogeochemical Elemental Cycling (BEC, Moore et al., 2004) component of the Community Earth System Model. Using a different biogenic prior flux from truth effectively avoids the optimistic conclusions that arise from assuming a perfect baseline. We seek to determine whether satellite observations will constrain the perturbation over and above the uncertainty in the biogenic emissions.

The prior flux uncertainty for all experiments assumes independence between the different flux categories. As in Baker et al. (2010), the prior uncertainty for the biosphere and ocean fluxes is taken to be the

absolute gridded uncertainty between the biased and unbiased baseline fluxes. The fossil fuel and fire emissions are not optimized. The prior uncertainty for the perturbations is described below.

2.3.2. Fossil Fuel Emissions Pattern Shift

As in H15, the sensitivity of ASCENDS and OCO-2 to potential shifts in anthropogenic emissions is tested using a hypothetical transition of emissions from Europe to China over the course of a decade. The shift is flux neutral so that the net global change is 0 and hence would not be detectable from an isolated remote site such as Mauna Loa. The net gain (loss) in emissions for China (Europe) is about 200 Tg C for the year, which corresponds to the lower signal scenario from H15. This scenario was found to be not detectable in H15 with up to 1 year's sampling in the presence of observational errors.

This scenario tests the satellite observing systems in two important ways. First, the test serves as a proxy for the ability of the instrument to constrain regional fluxes in the midlatitudes. Second, the regions are not homogenous, since the CALIPSO data for 2007 have much larger column ODs over China than over Europe (not shown). This manifests in the pseudo data sets as a reduction in the number of observations over China and larger uncertainties for the observations that meet the OD requirements due to the reduced signal arising from greater attenuation by scatterers. This means that we expect a better flux estimate over Europe than over China. Alternately, Europe is at a higher latitude than China, and so visibility limitations for OCO-2 are expected to make posterior flux errors larger in the NH winter and neighboring months.

The gridded 1° prior uncertainty for this perturbation is taken to be 25% of the V2015 $1^\circ \times 1^\circ$ gridded estimates (at grid scale) from the Carbon Dioxide Information Analysis Center (CDIAC). Although this fossil fuel uncertainty is small compared to current best estimates (Andres et al., 2016), we take a conservative approach given expected improvements in inventories in the next 5–10 years. As mentioned above, we take the prior flux uncertainty for the baseline flux components to be the absolute gridded difference between the biased and unbiased prior emissions.

2.3.3. Permafrost

The case for release of carbon to the atmosphere as a result of thawing permafrost is discussed in detail in H15. Briefly, the experiment uses projections of CO₂ fluxes from thawing permafrost from Schaefer et al. (2011). These fluxes are derived using the SiB-CASA land surface model (Schaefer et al., 2008), driven by climate model output under the A1B emissions scenario from the Intergovernmental Panel on Climate Change Fourth Assessment report. The fluxes used here are those for the year 2022, and the total perturbation is about 752 Tg C for that year. The prior uncertainty taken for the permafrost perturbation is 100% of the permafrost signal.

The high-latitude nature of this flux perturbation is expected to favor the active instrument due to its year-round coverage versus the seasonal coverage of OCO-2 visible in Figure 2.

2.3.4. Southern Ocean Interannual Variability

Doney et al. (2009) demonstrated that the Southern Ocean potentially has a large interannual variability and that in this region the ocean can change from being largely a source to largely a sink, as was the case in model years 1977 and 1979. The Southern Ocean is frequently obscured from space by clouds, making satellite-borne remotely sensed observations difficult. In addition, the flux signal is spread over a large region, making spatial signatures very small. These two factors make source/sink attribution challenging. In H15, it was found that the signal was too weak over short time periods to see significance, while for longer averaging periods the spatial pattern was smoothed out, leading to the conclusion that constraining the spatial pattern of emissions from space would be difficult. We utilize the difference between the climatological BEC fluxes and Takahashi fluxes as a test to see whether spaceborne observations will be able to constrain fluxes over the Southern Ocean. The prior uncertainty was taken to be the baseline prior uncertainty, as this experiment is in line with the uncertainty expressed by the difference in the BEC model output and Takahashi ocean fluxes.

2.4. Experimental Procedure

The first set of experiments utilizes the unbiased baseline as truth and the biased baseline as prior. The posterior constraint on this flux error is seen as the ability of the instruments to reduce the biogenic uncertainty. In particular, the results of these experiments are utilized for the Southern Ocean experiment. The fossil fuel and permafrost perturbation experiments use the unbiased baseline along with the appropriate perturbation as the truth.

For each case, the experiments were performed according to the following procedure:

1. Simulate X_{CO_2} pseudodata for each instrument using the truth fluxes for the time period 1 January 2014 to 1 April 2015 and the instrument-specific ground track and weighting function.
2. For each instrument, perform inversions using TM5-4DVar with observational uncertainties as described in section 2.2 with the biased prior and null perturbation.
3. Compute regional flux prior and posterior errors and posterior uncertainty using equation (8) of Meirink et al. (2008).

2.5. Success Criteria

In each of the perturbation experiments, the goals are to (1) reject the null hypothesis that the perturbations are 0 (i.e., a 1σ confidence interval about the posterior mean does not contain the prior mean) and (2) to provide a good estimate of the actual perturbation, where good means that the truth is inside a confidence interval about the posterior mean. These two objectives are not mutually exclusive, and so we report on them independently as two measures of success. Naturally, the preferred outcome is accomplishing both, at which point we will say the perturbation is detected. In the case of seasonal fluxes, we will report success if the goal is achieved for two out of four seasons. We will declare the perturbation detectable at the seasonal scale if both of the secondary goals are achieved for the *same* two months.

3. Results and Discussion

In this section, we present the results of the OSSEs described in section 2. The information content of pseudodata is assessed by comparing flux error statistics before and after assimilation of pseudodata. The flux error contains both a mean component and an uncertainty, which is computed from equation (8) of Meirink et al. (2008) for a given spatial region and temporal average and takes into account spatial and temporal correlations.

3.1. Baseline Emissions

As a first step, we apply the method to the recovery of the true baseline fluxes without perturbations. The annual flux errors, (prior flux – true flux) or (posterior flux – true flux), for the 22 Transcom regions (Gurney et al., 2002) are given in Figures S1 and S3 in the supporting information to give a sense of the ability of the different observations to constrain regional land and ocean fluxes. The seasonal flux errors for the baseline experiments are shown in Figures S2 and S4. The prior differences in this case represent the difference between the SiB4 and CASA terrestrial biosphere emissions, or the Takahashi and BEC emissions for the ocean regions. The general pattern, which is similar for most regions, is that ASCENDS provides a stronger constraint than OCO-2 on annual terrestrial emissions for the 2P and 4P cases and that the higher precision also leads to stronger constraints and lower posterior uncertainties. Further, the posterior uncertainties are similar for the WCO2 instrument and the SCO2 instrument, even though the observation errors are generally larger for the SCO2 instrument. The active measurements constrain terrestrial emissions at high latitudes more strongly than OCO-2, and at sufficiently high precision, they constrain most regions more strongly than OCO-2 year round. Ocean emissions have a similar pattern in mean flux errors, though the truth in all cases except the temperate Pacific and Atlantic is not within a 1σ confidence interval of the posterior emissions. Even though the fluxes (and corresponding flux errors) are much smaller than the terrestrial fluxes, the ability of ASCENDS to reduce the error relative to the prior is quite strong relative to OCO-2 but varies sharply with precision.

These results set the stage for the perturbation experiments in the following sections, and the outcome in each case is examined in this context.

3.2. Southern Ocean Flux Uncertainty

The Southern Ocean is extremely difficult to observe from space, due to regular widespread cloudiness. This consideration is factored into our OSSEs through cloud-screened OCO-2 observations and the use of CALIPSO ODs for ASCENDS. Figure 5 shows the aggregated prior and posterior annual errors for the Southern Ocean basin. All satellite observations constrain fluxes that improve upon the prior in terms of mean error, with the ASCENDS 4P observations providing a $> 60\%$ reduction. OCO-2 provides a $\sim 15\%$ reduction in the annual mean error.

This experiment differs from the other two in that none of the posterior distributions contain the truth within a 1σ confidence interval. The implication is that none of the instruments are sufficient to constrain the annual

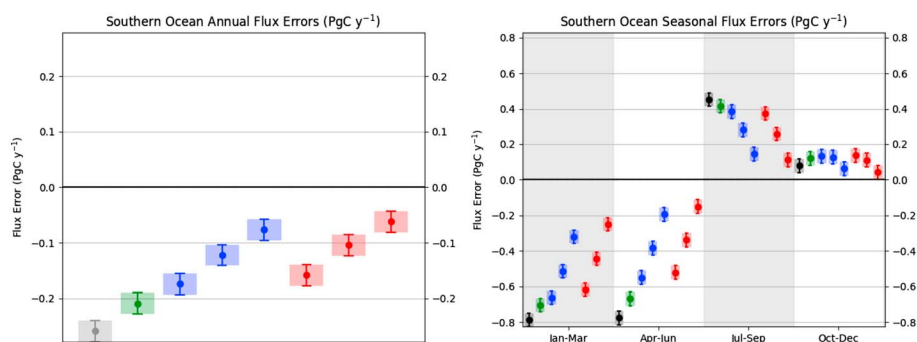


Figure 5. (left) Annual and (right) seasonal prior errors and posterior errors for the Southern Ocean region in the baseline experiment. The bars represent the 1σ uncertainty about the mean flux. The colors represent the prior (gray) and posterior errors after assimilating observations from OCO-2 (green), ASCENDS WCO₂ (blue), and ASCENDS SCO₂ (red). For the ASCENDS experiments, the precisions increase from 1P (left) to 2P (middle) to 4P (right). The prior uncertainty consists of the net flux prior uncertainty standard deviation as discussed in the text.

mean flux over the Southern Ocean, though the higher-precision ASCENDS instruments are able to reduce the error significantly more than the passive instruments like OCO-2.

3.3. Fossil Fuel Emissions Pattern Shift

In H15, the authors concluded that this “low signal” case would not be detectable in the presence of observational noise over a 1 year time period. The 4DVar technique avoids the spatiotemporal averaging inherent in the approach utilized in H15 and thereby leads to stronger conclusions. The annual and seasonal flux errors, (prior flux – true flux) or (posterior flux – true flux), are displayed in Figure 6. The bars represent an interval of

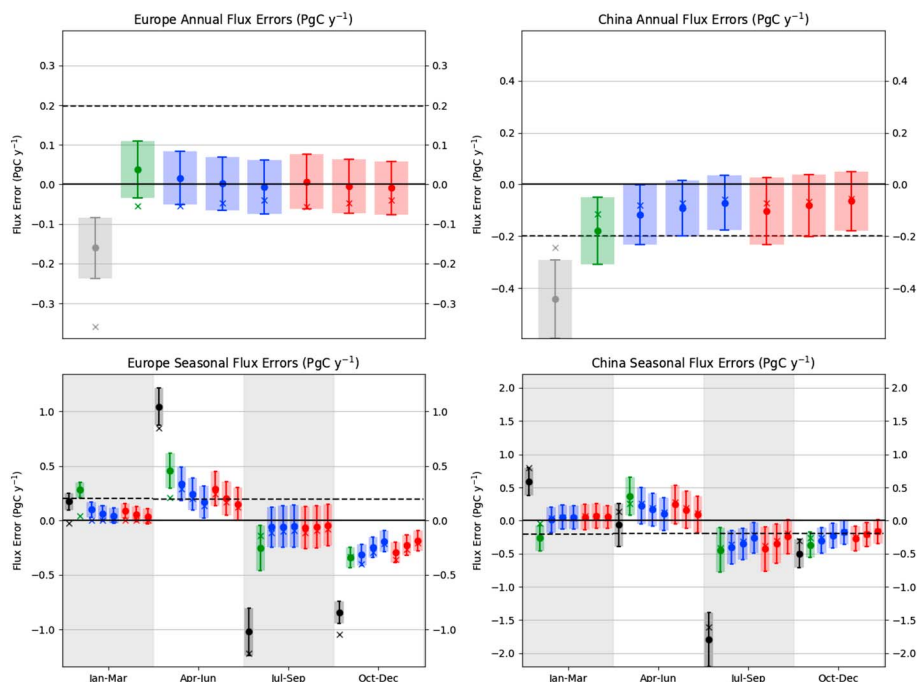


Figure 6. (top row) Annual and (bottom row) seasonal errors in the fossil fuel shift scenario prior emissions, as well as the posterior emissions after assimilating each of the pseudo data sets as indicated by the legend. The bars represent the 1σ uncertainty about the mean flux. The X markers represent the baseline prior and posterior flux errors. The colors represent the prior (gray), OCO-2 (green), ASCENDS WCO₂ (blue), and ASCENDS SCO₂ (red). For the ASCENDS experiments, the precisions increase from 1P (left) to 2P (middle) to 4P (right). The prior uncertainty consists of the net flux prior uncertainty standard deviation as discussed in the text. The dashed horizontal line is the flux perturbation in the absence of biogenic flux error.

Table 1
Outcomes for Fossil Fuel Shift Detection at the Annual Time Scale

Region	Goal	OCO-2	WCO2			SCO2		
			1P	2P	4P	1P	2P	4P
Europe	Reject H0	✓	✓	✓	✓	✓	✓	✓
	Estimate truth	✓	✓	✓	✓	✓	✓	✓
	Detect pert	✓	✓	✓	✓	✓	✓	✓
China	Reject H0				✓			✓
	Estimate truth			✓	✓	✓	✓	✓
	Detect pert				✓			✓

Note. Check mark means the goal was achieved.

one standard deviation around the prior and posterior errors, denoted by the filled circles. The X markers represent the prior and posterior mean flux errors from the baseline experiment (section 3.1) and are included to highlight the effects of prior errors on the results. Examining the differences between the circle and X markers, it is clear that the ASCENDS posterior errors for both the baseline and perturbation experiments are closer to 0 (and to each other) than the OCO-2 cases. This implies that the ASCENDS results are less sensitive to prior errors, which is a natural consequence of the greater coverage of the active instrument.

The annual flux error statistics are depicted in Figure 6 (top row). All experiments shift the annual mean flux toward the truth (i.e., the error toward 0) for both regions. The posterior uncertainty for China is about twice that of the uncertainties for Europe for all experiments, which is representative of larger measurement errors and a larger prior uncertainty arising from the biospheric differences between SiB and CASA. The ASCENDS WCO2 posterior flux uncertainties are smaller than SCO2 for all precisions. For all of the ASCENDS cases, SCO2 has a stronger mean error reduction than WCO2, though this result is not statistically significant. The European annual true emissions fall between the satellite estimates $\pm 1\sigma$ so that a hypothesis test with the assumption of a zero perturbation would be rejected at 1σ confidence level. This result is weaker for China (due to the larger prior errors and measurement errors), where only the 4P ASCENDS instruments would be able to reject the null perturbation hypothesis at the 1σ confidence level (Table 1), though all but the WCO2 1P case contains the truth in a 1σ confidence interval.

The seasonal errors are displayed in Figure 6 (bottom row). In general, the OCO-2 posterior errors are more strongly influenced by the prior, which arises from fewer observations in the regions of interest. Looking at Europe, the ASCENDS 2P and 4P cases are able to reject the null perturbation hypothesis at the 1σ confidence level during the January–March period due to the relatively small prior errors, but only the SCO2 4P instrument is sufficient in the April–June period due to larger prior errors. All active instruments are roughly equivalent for Europe in the summer months, and all produce posterior fluxes that reject the null perturbation hypothesis at the 1σ confidence level. The Chinese seasonal flux errors demonstrate the difficulty of constraining a small perturbation in a polluted region. During the first half of the year, the prior errors are small relative to the perturbation, and so the active instruments are able to successfully capture the perturbation. In

Table 2
Outcomes for Fossil Fuel Shift Detection at the Seasonal Time Scale

Region	Goal	OCO-2	WCO2			SCO2		
			1P	2P	4P	1P	2P	4P
Europe	Reject H0	✓	✓	✓	✓	✓	✓	✓
	Estimate truth			✓	✓		✓	✓
	Detect pert			✓	✓		✓	✓
China	Reject H0		✓	✓	✓	✓	✓	✓
	Estimate truth		✓	✓	✓	✓	✓	✓
	Detect pert		✓	✓	✓	✓	✓	✓

Note. Check mark means the goal was achieved. For the “detect pert” row, success is only achieved if the two secondary goals are achieved in the same two seasons.

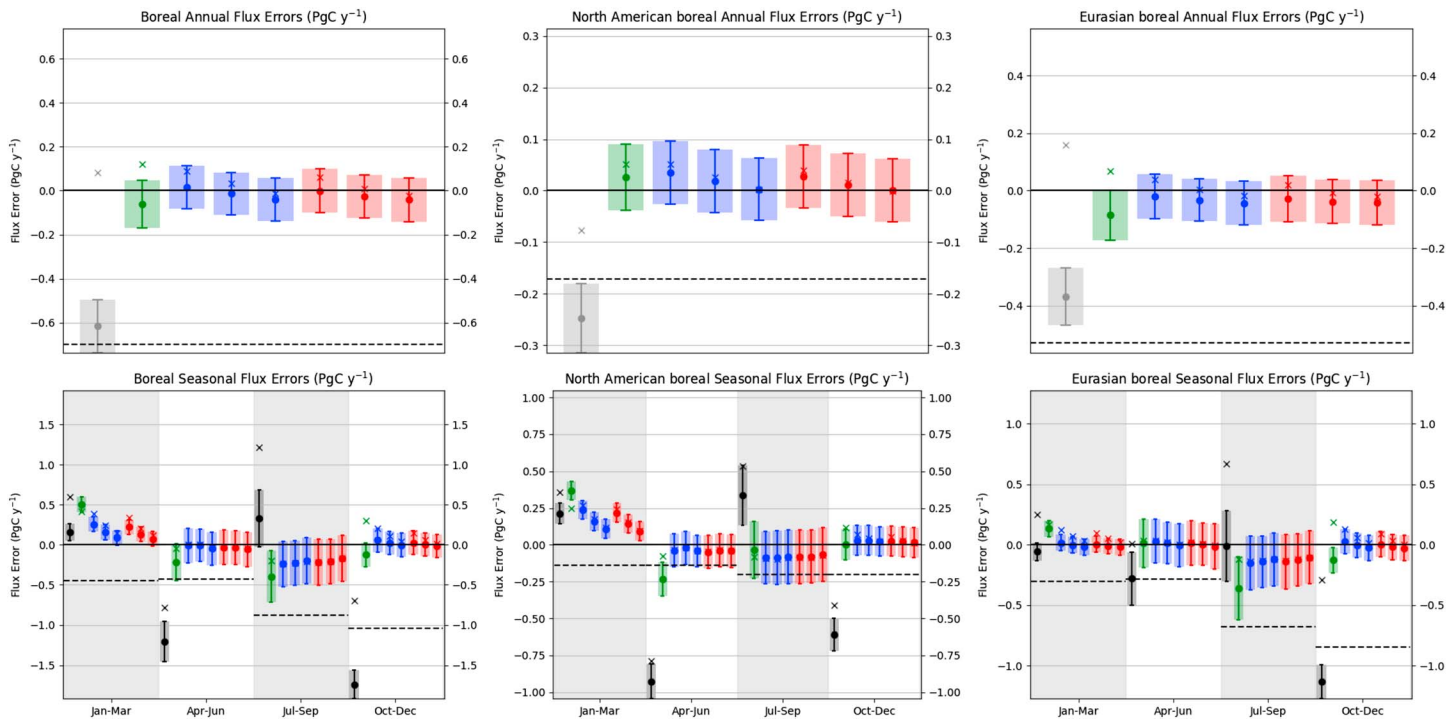


Figure 7. (top row) Annual and (bottom row) seasonal errors for the permafrost perturbation experiment. (left column) The flux errors for the boreal land region and the flux errors for the (middle column) North American boreal and (right column) Eurasian boreal regions. The bars represent the a 1σ uncertainty about the mean flux. The X markers represent the prior and posterior flux errors from the baseline experiment. The colors represent the prior (gray), OCO-2 (green), ASCENDS WCO₂ (blue), and ASCENDS SCO₂ (red). For the ASCENDS experiments, the precisions increase from 1P (left) to 2P (middle) to 4P (right).

the second half of the year, only the SCO₂ 4P instrument is able to do so. OCO-2 is unable to constrain the regional perturbations in any season due to its sensitivity to the prior error magnitude (Table 2).

3.4. Permafrost Thaw

The case of thawing permafrost is interesting as a discriminant between the capabilities of passive and active missions. The year-round high-latitude sensing capability of ASCENDS improves detection of concentration anomalies (and hence flux anomalies) in the fall-winter-spring months. The large-scale errors are computed for the North American boreal and Eurasian boreal regions as defined for the TransCom project (e.g., boreal North America and boreal Asia in Figure 7 of Gurney et al., 2003).

Table 3
Outcomes for Permafrost Thaw Detection at the Annual Time Scale

Region	Goal	OCO-2	WCO ₂			SCO ₂		
			1P	2P	4P	1P	2P	4P
North American boreal	Reject H0	✓	✓	✓	✓	✓	✓	✓
	Estimate truth	✓	✓	✓	✓	✓	✓	✓
	Detect pert	✓	✓	✓	✓	✓	✓	✓
European boreal	Reject H0	✓	✓	✓	✓	✓	✓	✓
	Estimate truth	✓	✓	✓	✓	✓	✓	✓
	Detect pert	✓	✓	✓	✓	✓	✓	✓
Boreal	Reject H0	✓	✓	✓	✓	✓	✓	✓
	Estimate truth	✓	✓	✓	✓	✓	✓	✓
	Detect pert	✓	✓	✓	✓	✓	✓	✓

Note: Check mark means the goal was achieved.

Table 4
Outcomes for Permafrost Thaw Detection at the Seasonal Time Scale

Region	Goal	OCO-2	WCO2			SCO2		
			1P	2P	4P	1P	2P	4P
North American boreal	Reject H0	✓	✓	✓	✓	✓	✓	✓
	Estimate truth		✓	✓	✓	✓	✓	✓
	Detect pert							
European boreal	Reject H0	✓	✓	✓	✓	✓	✓	✓
	Estimate truth		✓	✓	✓	✓	✓	✓
	Detect pert		✓	✓	✓	✓	✓	✓
Boreal	Reject H0	✓	✓	✓	✓	✓	✓	✓
	Estimate truth	✓	✓	✓	✓	✓	✓	✓
	Detect pert		✓	✓	✓	✓	✓	✓

Note. Check mark means the goal was achieved. For the “detect pert” row, success is only achieved if the two secondary goals are achieved in the same two seasons.

The annual and seasonal flux errors are shown in Figure 7 for the boreal Transcom regions, using the same color scheme as in Figure 6. The North American boreal region is depicted in Figure 7 (middle column), the Eurasian boreal region is depicted in Figure 7 (right column), and their sum in Figure 7 (left column). This perturbation has a larger annual flux signal than the fossil fuel shift experiment, and so we expect that the mean error reductions will be larger. As seen in Figure 7, this is the case. In both regions, all experiments reduce the annual sum posterior mean error so that the null permafrost perturbation hypothesis can be rejected at the 2σ confidence level, and in the Eurasian boreal, it can be rejected at the 3σ level for the annual total flux. Since the posterior error confidence intervals all also contain the true mean flux, the annual permafrost thaw flux signal is found to be detectable in both regions. Similarly, the perturbation for the entire boreal region taken as a whole is detectable (Table 3).

Examining the seasonal flux errors, which is an important aspect of attribution, the impacts of the biological uncertainty during the growing season become important. Even though all instruments reject the null hypothesis for two seasons in boreal North America, they fail to capture the truth in winter due to the relatively small perturbation signal. This means that the boreal permafrost signal in North America is not detectable at the seasonal scale. In boreal Eurasia, the active instruments are able to successfully detect the perturbation, but OCO-2 fails to capture the truth in three of the four seasons, and so it cannot detect the perturbation. The results for the boreal forests taken together match those of the Eurasian boreal region, and OCO-2 is unable to constrain the seasonal flux over the region even taken as whole (Table 4).

4. Conclusions and Future Work

The OSSEs presented here suggest that the space-based observing capabilities have the potential to constrain annual CO_2 fluxes even in the presence of transport and representativeness errors. They also point to the need for more complete coverage over all seasons, in this case being provided by active remote sensing measurements of CO_2 like those provided by ASCENDS, to provide constraints at higher time resolution, particularly in high latitudes and over polluted regions. The more interesting finding is that there is not a simple relationship between coverage and overall constraint, as errors arise from the misspecification of the biospheric fluxes and their associated uncertainty. Thus, even though coverage is poorer in the winter-time, the posterior errors are not necessarily worse than the other seasons due to the confounding factor of the biospheric flux errors.

The observational errors chosen for the different instruments reflect the current best estimate of the expected (for ASCENDS) or actual (for OCO-2) measurement uncertainty in observation, although this error is underestimated due to the absence of systematic observation errors. Systematic errors were also not included in the OCO-2 analysis, though Eldering et al. (2017) suggest that systematic errors for OCO-2 retrievals could be more than 1 ppm in certain regions, such as the southern high latitudes.

The fossil fuel shift scenario shows that even in the midlatitudes, attributing sources in the presence of uncertain biospheric fluxes is difficult. The annual time scale is well constrained for Europe by all instruments but

not by OCO-2 for China due to poorer coverage and larger posterior errors from aerosol pollutants. On seasonal time scales, the active instruments show strong potential to constrain fluxes, assuming that the instrument precision is high enough.

NH high latitude emissions have been the focus of numerous field campaigns in recent years, such as the Carbon in Arctic Reservoirs Vulnerability Experiment (CARVE) and Arctic Boreal Vulnerability Experiment (ABOVE). Though the understanding of the drivers of emissions is growing with these campaigns, there is still large uncertainty in the interannual variability, as well as the long-term dynamics of the region as the climate warms. ASCENDS shows strong potential for detecting and attributing Arctic emissions in the NH, particularly in the post-summer active season when release continues even with reduced insolation. Though this hypothesis specifically targeted permafrost release, the OSSEs also imply that ASCENDS would constrain high-latitude fluxes all year long, which would increase our understanding of potentially fragile boreal ecosystems and how they respond to climate shifts.

The Southern Ocean is the most challenging of the three scenarios, due to the spatially diffuse flux signal, perennial cloudiness, and large interannual variability. Though not tested here, inversions in this region also suffer from sparse meteorological observations that drive transport model capabilities (and hence larger transport uncertainty). While none of the experiments produced a posterior flux mean that agreed with the true Southern Ocean flux, the active instruments showed a strong ability to move the errors closer to 0.

These results affirm the findings of H15 regarding the capabilities of a space-based active system and demonstrate the strength of the full transport inversion to infer flux variations in space and time. The next step for this work is to provide realistic estimates of systematic biases for the two measurement concepts and OCO-2, as well as estimates of transport error with spatial coherence, and to extend these simulations to assess their impact. A proper characterization of biases will be aided by ongoing aircraft campaigns for ASCENDS and operations for OCO-2.

Acknowledgments

S. M. C. acknowledges support from NASA award NNX15AJ27G. S. C. D. acknowledges support from NASA award NNX15AH13G. All data displayed in this study are available for download at http://seanrowell.oucreate.com/flux_pert.tgz.

References

- Abshire, J., Ramanathan, A., Riris, H., Mao, J., Allan, G., Hasselbrack, W., ... Browell, E. (2014). Airborne measurements of CO₂ column concentration and range using a pulsed direct-detection IPDA lidar. *Remote Sensing*, 6, 443–469.
- Abshire, J., Riris, H., Allan, G. R., Weaver, C. J., Mao, J., Sun, X., ... Biraud, S. (2010). Pulsed airborne lidar measurements of atmospheric CO₂ column absorption. *Tellus B*, 62, 770–783.
- Andres, R. J., Boden, T. A., & Higdon, D. M. (2016). Gridded uncertainty in fossil fuel carbon dioxide emission maps, a CDIAC example. *Atmospheric Chemistry and Physics*, 16, 14,979–14,995. <https://doi.org/10.5194/acp-16-14979-2016>
- Babenhauserheide, A., Basu, S., Houweling, S., Peters, W., & Butz, A. (2015). Comparing the carbon tracker and TM5-4DVAR data assimilation systems for CO₂ surface flux inversions. *Atmospheric Chemistry and Physics*, 15(17), 9747–9763. <https://doi.org/10.5194/acp-15-9747-2015>
- Baker, D. F., Boesch, H., Doney, S. C., O'Brien, D., & Schimel, D. (2010). Carbon source/sink information provided by column CO₂ measurements from the Orbiting Carbon Observatory. *Atmospheric Chemistry and Physics*, 10, 4145–4165.
- Basu, S., Guerlet, S., Butz, A., Houweling, S., Hasekamp, O., Aben, I., ... Worthy, D. (2013). Global CO₂ fluxes estimated from GOSAT retrievals of total column CO₂. *Atmospheric Chemistry and Physics*, 13, 8695–8717.
- Boesch, H., Baker, D., Connor, B., Crisp, D., & Miller, C. (2011). Global characterization of CO₂ column retrievals from shortwave-infrared satellite observations of the Orbiting Carbon Observatory-2 Mission. *Remote Sensing*, 3(2), 270–304.
- Browell, E. V., Dobbs, M. E., Dobler, J., Kooi, S., Choi, Y., Harrison, F. W., ... Zaccheo, T. S. (2008). Airborne demonstration of 1.57-micron laser absorption spectrometer for atmospheric CO₂ measurements, Proc. of 24th International Laser Radar Conference, S06P-13, Boulder, CO, June 23–27.
- Browell, E. V., Dobbs, M., Dobler, J., Kooi, S., Choi, Y., Harrison, F. W., ... Zaccheo, T. S. (2009). First airborne laser remote measurements of atmospheric CO₂ for future active sensing of CO₂ from space, Proc., 8th International Carbon Dioxide Conference, Jena, Germany, September 13–18.
- Browell, E. V., Dobler, J., Kooi, S., Choi, Y., Harrison, F. W., Moore, B. III, & Zaccheo, T. S. (2010). Airborne validation of laser remote measurements of atmospheric CO₂, Proc., 25th International Laser Radar Conference, S6O-03, St. Petersburg, Russia, July 5–9.
- Chevallier, F., Feng, L., Boesch, H., Palmer, P., & Rayner, P. (2010). On the impact of transport model errors for the estimation of CO₂ surface fluxes from GOSAT observations. *Geophysical Research Letters*, 37, L21803. <https://doi.org/10.1029/2010GL044652>
- Corbin, K. D., Denning, A. S., Lu, L., Wang, J.-W., & Baker, I. T. (2008). possible representation errors in inversions of satellite CO₂ retrievals. *Journal of Geophysical Research*, 113, D02301. <https://doi.org/10.1029/2007JD008716>
- Crisp, D., Atlas, R. M., Breon, F. M., Brown, L. R., Burrows, J. P., Ciais, P., ... Schroll, S. (2004). The Orbiting Carbon Observatory (OCO) mission. *Advances in Space Research*, 34(4), 700–709.
- Dee, D. P., Uppala, S. M., Simmons, A. J., Berrisford, P., Poli, P., Kobayashi, S., ... Vitart, F. (2011). The ERA-Interim reanalysis: Configuration and performance of the data assimilation system. *Quarterly Journal of the Royal Meteorological Society*, 137, 553–597. <https://doi.org/10.1002/qj.828>
- Dobler, J., Harrison, F. W., Browell, E. V., Lin, B., McGregor, D., Kooi, S., ... Ismail, S. (2013). Atmospheric CO₂ column measurements with an airborne Intensity-modulated continuous wave 1.57 μm. *Fiber Laser Lidar, Applied Optics*, 52(12), 2874–2892.
- Doney, S. C., Lima, I., Feely, R. A., Glover, D. M., Lindsay, K., Mahowald, N., ... Wanninkhof, R. (2009). Mechanisms governing interannual variability in upper-ocean inorganic carbon system and air-sea CO₂ fluxes: Physical climate and atmospheric dust. *Deep Sea Research, Part II*, 56(8–10), 640–655. <https://doi.org/10.1016/j.dsr2.2008.12.006>

- Eldering, A., O'Dell, C. W., Wennberg, P. O., Crisp, D., Gunson, M. R., Viatte, C., ... Yoshimizu, J. (2017). The Orbiting Carbon Observatory-2: First 18 months of science data products. *Atmospheric Measurement Techniques*, 10, 549–563. <https://doi.org/10.5194/amt-10-549-2017>
- Engelen, R. J., Denning, A. S., Gurney, K. R., & TransCom3 modelers (2002). On error estimation in atmospheric CO₂ inversions. *Journal of Geophysical Research*, 107(D22), 4635. <https://doi.org/10.1029/2002JD002195>
- Friedlingstein, P., Meinshausen, M., Arora, V. K., Jones, C. D., Anav, A., Liddicoat, S. K., & Knutti, R. (2014). Uncertainties in CMIP5 climate projections due to carbon cycle feedbacks. *Journal of Climate*, 27, 511–526. <https://doi.org/10.1175/JCLI-D-12-00579.1>
- Garnier, A., Pelon, J., Dubuisson, P., Faivre, M., Chomette, O., Pascal, N., & Kratz, D. P. (2012). Retrieval of cloud properties using CALIPSO imaging infrared radiometer. Part I: Effective emissivity and optical depth. *Journal of Applied Meteorology and Climatology*, 51(7), 1407–1425. <https://doi.org/10.1175/JAMC-D-11-0220.1>
- Gurney, K. R., Law, R. M., Denning, A. S., Rayner, P. J., Baker, D., ... Yuen, C. W. (2003). Transcom 3 CO₂ inversion intercomparison: 1. Annual mean control results and sensitivity to transport and prior flux information. *Tellus*, 55B, 555–579.
- Gurney, K. R., Law, R. M., Denning, A. S., Rayner, P. J., Baker, D., Bousquet, P., ... Yuen, C. W. (2002). Towards robust regional estimates of CO₂ sources and sinks using atmospheric transport models. *Nature*, 415, 626–630.
- Hammerling, D. M., Kawa, S. R., Schaefer, K., Doney, S., & Michalak, A. M. (2015). Detectability of CO₂ flux signals by a space-based lidar mission. *Journal of Geophysical Research: Atmospheres*, 120, 1794–1807. <https://doi.org/10.1002/2014JD022483>
- Hu, Y., Stamnes, K., Vaughan, M., Pelon, J., Weimer, C., Wu, D., ... Santa-Maria, M. (2008). Sea surface wind speed estimation from space-based lidar measurements. *Atmospheric Chemistry and Physics*, 8(13), 3593–3601. <https://doi.org/10.5194/acp-8-3593-2008>
- Hunt, W. H., Winker, D. M., Vaughan, M. A., Powell, K. A., Lucker, P. L., & Weimer, C. (2009). CALIPSO lidar description and performance assessment. *Journal of Atmospheric and Oceanic Technology*, 26(7), 1214–1228. <https://doi.org/10.1175/2009JTECHA1223.1>
- Jucks, K. W., Neeck, S., Abshire, J. B., Baker, D. F., Browell, E. V., Chatterjee, A., ... Zaccheo, T. S. (2015). Active Sensing of CO₂ Emissions over Nights, Days, and Seasons (ASCENDS) mission: Science mission definition study. Retrieved from http://cce.nasa.gov/ascends_2015/ASCENDS_FinalDraft_4_27_15.pdf
- Kawa, S. R., Mao, J., Abshire, J. B., Collatz, G. J., Sun, X., & Weaver, C. (2010). Simulation studies for a space-based CO₂ lidar mission. *Tellus B*, 62(5), 759–769.
- Krol, M., Houweling, S., Bregman, B., van den Broek, M., Segers, A., van Velthoven, P., ... Bergamaschi, P. (2005). The two-way nested global chemistry–transport zoom model TM5: Algorithm and applications. *Atmospheric Chemistry and Physics*, 5, 417–432.
- Kulawik, S., Wunch, D., O'Dell, C., Frankenberg, C., Reuter, M., Oda, T., ... Wolf, J. (2015). Consistent evaluation of ACOS-GOSAT, BESD-SCIAMACHY, CARBONTRACKER, and MACC through comparisons to TCCON. *Atmospheric Measurement Techniques*, 9, 683–709. <https://doi.org/10.5194/amt-9-683-2016>
- Kuze, A., Suto, H., Shiomi, K., Kawakami, S., Tanaka, M., Ueda, Y., ... Buijs, H. L. (2016). Update on GOSAT TANSO-FTS performance, operations, and data products after more than 6 years in space. *Atmospheric Measurement Techniques*, 9, 2445–2461. <https://doi.org/10.5194/amt-9-2445-2016>
- Lin, B., Nehrir, A. R., Harrison, F. W., Browell, E. V., Ismail, S., Obland, M. D., ... Kooi, S. (2015). Atmospheric CO₂ column measurements in cloudy conditions using intensity-modulated continuous-wave lidar at 1.57 micron. *Optics Express*, 23. <https://doi.org/10.1364/OE.23.00A582>
- Mao, J., Ramanathan, A., Abshire, J. B., Kawa, S. R., Riris, H., Allan, G. R., ... Yang, M. Y. M. (2018). Measurement of atmospheric CO₂ column concentrations to cloud tops with a pulsed multi-wavelength airborne lidar. *Atmospheric Measurement Techniques*, 11, 127–140. <https://doi.org/10.5194/amt-11-127-2018>
- Meirink, J. F., Bergamaschi, P., & Krol, M. C. (2008). Four-dimensional variational data assimilation for inverse modeling of atmospheric methane emissions: Method and comparison with synthesis inversion. *Atmospheric Chemistry and Physics*, 8, 6341–6353. <https://doi.org/10.5194/acp-8-6341-2008>
- Menzies, R. T., Spiers, G. D., & Jacob, J. (2013). Airborne laser absorption spectrometer measurements of atmospheric CO₂ column mole fractions: Source and sink detection and environmental impacts on retrievals. *Journal of Atmospheric and Oceanic Technology*, 31(2), 404–421. <https://doi.org/10.1175/JTECH-D-13-00128.1>
- Miller, C. E., Crisp, D., DeCola, P. L., Olsen, S. C., Randerson, J. T., Michalak, A. M., ... Law, R. M. (2007). Precision requirements for space-based data. *Journal of Geophysical Research*, 112, D10314. <https://doi.org/10.1029/2006JD007659>
- Moore, J. K., Doney, S. C., & Lindsay, K. (2004). Upper ocean ecosystem dynamics and iron cycling in a global three-dimensional model. *Global Biogeochemical Cycles*, 18, GB4028. <https://doi.org/10.1029/2004GB002220>
- National Aeronautics and Space Administration (2015). Orbiting Carbon Observatory-2 warn level, bias correction and lite file product description v1.1. Retrieved from http://disc.sci.gsfc.nasa.gov/OCO-2/documentation/oco-2-v7/OCO2_XCO2_Lite_Files_and_Bias_Correction.pdf
- National Research Council (2007). Earth science and applications from space: National imperatives for the next decade and beyond, Tech. rep., National Research Council.
- Oda, T., & Maksyutov, S. (2011). A very high-resolution (1 km x 1 km) global fossil fuel CO₂ emission inventory derived using a point source database and satellite observations of nighttime lights. *Atmospheric Chemistry and Physics*, 11, 543–556. <https://doi.org/10.5194/acp-11-543-2011>
- O'Dell, C. W., Connor, B., Boesch, H., O'Brien, D., Frankenberg, C., Castano, R., ... Wunch, D. (2012). The ACOS CO₂ retrieval algorithm—Part 1: Description and validation against synthetic observations. *Atmospheric Measurement Techniques*, 5(1), 99–121. <https://doi.org/10.5194/amt-5-99-2012>
- Peters, W., Jacobson, A. R., Sweeney, C., Andrews, A. E., Conway, T. J., Masarie, K., ... Tans, P. P. (2007). An atmospheric perspective on North American carbon dioxide exchange: Carbontracker. *Proceedings of the National Academy of Sciences of the United States of America*, 104(48), 18,925–18,930. <https://doi.org/10.1073/pnas.0708986104>
- Ramanathan, A. K., Mao, J., Abshire, J. B., & Allan, G. R. (2015). Remote sensing measurements of the CO₂ mixing ratio in the planetary boundary layer using cloud slicing with airborne lidar. *Geophysical Research Letters*, 42, 2055–2062. <https://doi.org/10.1002/2014GL062749>
- Rayner, P. J., & O'Brien, D. M. (2001). The utility of remotely sensed CO₂ concentration data in surface source inversions. *Geophysical Research Letters*, 28, 175–178. <https://doi.org/10.1029/2000GL011912>
- Schaa, C. B., Gao, F., Strahler, A. H., Lucht, W., Li, X., Tsang, T., ... Roy, D. (2002). First operational BRDF, albedo nadir reflectance products from MODIS. *Remote Sensing of Environment*, 83(1–2), 135–148. [https://doi.org/10.1016/S0034-4257\(02\)00091-3](https://doi.org/10.1016/S0034-4257(02)00091-3)
- Schaefer, K., Collatz, G. J., Tans, P., Denning, A. S., Baker, I., Berry, J., ... Philpott, A. (2008). Combined Simple biosphere/Carnegie-Ames-Stanford approach terrestrial carbon cycle model. *Journal of Geophysical Research*, 113, G03034. <https://doi.org/10.1029/2007JG000603>
- Schaefer, K., Zhang, T., Bruhwiler, L., & Barrett, A. P. (2011). Amount and timing of permafrost carbon release in response to climate warming. *Tellus B*, 63, 165–180. <https://doi.org/10.1111/j.1600-0889.2011.00527.x>

- Spiers, G., Menzies, R. T., Jacob, J., Christensen, L. E., Phillips, M. W., Choi, Y., & Browell, E. V. (2011). Atmospheric CO₂ measurements with a 2 μm airborne laser absorption spectrometer employing coherent detection. *Applied Optics*, 50(14), 2098–2111.
- Takahashi, T., Sutherland, S. C., Wanninkhof, R., Sweeney, C., Feely, R. A., Chipman, D. W., ... de Baar, H. J. (2009). Climatological mean and decadal change in surface ocean pCO₂, and net sea–air CO₂ flux over the global oceans. *Deep Sea Research Part II: Topical Studies in Oceanography*, 56(8–10), 554–577. <https://doi.org/10.1016/j.dsr2.2008.12.009>
- Taylor, T. E., O'Dell, C. W., Frankenberg, C., Partain, P. T., Cronk, H. Q., Savtchenko, A., & Gunson, M. R. (2016). Orbiting Carbon Observatory-2 (OCO-2) cloud screening algorithms: Validation against collocated MODIS and CALIOP data. *Atmospheric Measurement Techniques*, 9, 973–989. <https://doi.org/10.5194/amt-9-973-2016>
- Wang, J. S., Kawa, S. R., Eluszkiewicz, J., Baker, D. F., Mountain, M., Henderson, J., ... Zaccheo, T. S. (2014). A regional CO₂ observing system simulation experiment for the ASCENDS satellite mission. *Atmospheric Chemistry and Physics*, 14(23), 12,897–12,914.
- Winker, D. M., Tackett, J. L., Getzewich, B. J., Liu, Z., Vaughan, M. A., & Rogers, R. R. (2013). The global 3-D distribution of tropospheric aerosols as characterized by CALIOP. *Atmospheric Chemistry and Physics*, 13(6), 3345–3361. <https://doi.org/10.5194/acp-13-3345-2013>
- Worden, J. R., Doran, G., Kulawik, S., Eldering, A., Crisp, D., Frankenberg, C., ... Bowman, K. (2017). Evaluation and attribution of OCO-2 XCO₂ uncertainties. *Atmospheric Measurement Techniques*, 10, 2759–2771. <https://doi.org/10.5194/amt-10-2759-2017>
- Wunch, D., Wennberg, P. O., Osterman, G., Fisher, B., Naylor, B., Roehl, C. M., ... Eldering, A. (2017). Comparisons of the Orbiting Carbon Observatory-2 (OCO-2) XCO₂ measurements with TCCON. *Atmospheric Measurement Techniques*, 10, 2209–2238. <https://doi.org/10.5194/amt-10-2209-2017>